Korean J. Chem. Eng., 33(10), 2830-2841 (2016)
DOI: 10.1007/s11814-016-0193-4

pISSN: 0256-1115
eISSN: 1975-7220

Simulation of solid-liquid flows using a two-way coupled smoothed particle hydrodynamics-discrete element method model

Jihoe Kwon† and Heechan Cho

Department of Energy and Resources Engineering, Seoul National University, 1 Gwanak-ro, Gwanak-gu, Seoul 08826, Korea
(*Received 10 January 2016 • accepted 2 July 2016*)

Abstract−We introduce a coupled smoothed particle hydrodynamics-discrete element method (SPH-DEM) to describe the two-way interaction between the two phases of a solid-liquid flow. To validate the model, we simulated two test problems: a solid-liquid counter-flow in a periodic box and particle settlement. The simulations correctly predicted the dynamics, and the results showed good agreement with the theory. The developed model was then applied to simulate the slurry coagulation process to examine the coagulation efficiency. When the rotational speed exceeded the normal range, the coagulation rate decreased with time, even though the rate was high during the early stage due to the size separation effect of the particles. Given this result, overly fast stirring appears to have an adverse effect on the coagulation efficiency. The model is applicable to the design of various types of solid-liquid flows.

Keywords: Solid-liquid Flow, SPH, DEM, Particle-laden Flow, Particle Method

INTRODUCTION

Owing to their high efficiency, solid-liquid two-phase flow systems are widely used for processes such as milling, separation, and material transportation. However, numerous difficulties are associated with the numerical and computational analyses of such systems. One of the most challenging problems is analyzing and modeling the interaction between the solid and liquid phases. The motion of solid particles affects the liquid flow and is in turn influenced by the flow fields through interactive effects. Therefore, moving particulate materials can be considered to impose an unsteady boundary condition on a fluid flow.

To simulate a solid-liquid two-phase flow, numerous studies have adopted a combined continuum and discrete model (CCDM) approach [1-6]. A CCDM describes solid particles by N-body using the discrete element method (DEM), while the flow is described by Eulerian grid-based hydrodynamics. This approach is applicable to problems in which the fluid length scale of interest is much greater than the particle diameter, so cells that are 10^1-10^3 times the size of the solid particles are generally used for flow analysis. Therefore, the influence of the motion of the solid particles on the flow can only be described on a macro-scale by averaging the properties over a grid. Another limitation of this approach is that analyses of flow problems involving moving boundary conditions, a free surface, and an unfixed fluid domain are still very difficult with the grid-based Eulerian approach.

Smoothed particle hydrodynamics (SPH) is a Lagrangian computational fluid dynamics (CFD) model. It was originally developed to solve astrophysical problems in the 1970s [7,8], but its application has been broadened to various areas of fluid-related computational physics. One of the most significant differences between SPH and Eulerian CFD is that the former traces material points without the use of a mesh. Because of this mesh-free property, SPH is highly applicable to problems involving complex fluid domains (e.g., free-surface flows or multiphase flows) while not imposing severe constraints, which are inevitable with a conventional grid-based model. Another advantage of SPH when modeling a solid-liquid flow is its potentially high compatibility with DEM. The motion of the fluid particles is tracked by a Lagrangian method through sequential calculation of the acceleration, velocity, and displacement, after which the positions of the fluid particles in the next time step are determined. This time propagation procedure of SPH is very similar to that of DEM. The similarity enables the use of one model to describe the interaction of particles from the other model in a consistent manner. These two different numerical models can therefore be combined without any conflict. However, the coupling of these two Lagrangian models generally requires a greater computational load than CCDM, although the difference is not too much.

A few works have coupled SPH and DEM to model the flow of a solid-liquid mixture. Potapov et al. [9] used SPH and DEM to simulate a solid-liquid flow. They coupled the two models by solving the solid particle motion with DEM and then analyzing the liquid phase with SPH by using the changed boundary information. They set up a macroscopic solid particle that is much larger than the mean inter-particle spacing of the SPH particles. Thus, owing to the heavy computational load, they could describe the motion of only a few solid particles. Cleary et al. [10] modeled the wet semi-autogenous (SAG) mill process by using SPH and DEM. They applied Darcy's law and the Kozeny-Carmen permeability relationship to the fluid based on the porosity and velocity distributions. They assumed the interaction to be one-way: the solid particles move in a steady state, and the slurry forces acting on the solid particles are negligible.

†To whom correspondence should be addressed.
E-mail: iori96@snu.ac.kr

Robinson et al. [11] conducted two-way coupling of SPH and DEM at the mesoscale. Their SPH fluid phase model is based on the locally averaged Navier-Stokes equations derived by Anderson and Jackson [12].

In this work, we introduce a new coupled SPH-DEM model. The main differences between our SPH model and that of Robinson et al. [11] are as follows:

1) Unlike existing models, the interaction term between the solid and liquid is directly evolved from the continuum equation without the use of any normalization such as the Shepard correction. Robinson et al.'s model uses a normalization procedure, and the interaction between a DEM particle and SPH particle changes depending on the manner in which the range of the support domain of the SPH particle is defined, which is undesirable. In our model, the influence of an individual solid particle on an SPH liquid particle is independent of the numerical configuration of the support domain, which eliminates this problem.

2) The interaction term is interpolated directly, whereas Robinson et al.'s model interpolates the interaction term consecutively from the interpolated pressure gradient and divergence of the stress tensor. Therefore, the numerical interpolation of the interaction in this model is more efficient than that of Robinson et al.'s model.

3) This work uses the equations of motion given by Harlow and Amsden [13,14], whereas Robinson et al. used the equations of motion given by Anderson and Jackson [12].

Our model considers the reduction of the flow domain due to the space occupied by the solid particles and the drag and pressure forces to describe the interaction between the two phases. To validate the model, we simulated two test problems: a solid-liquid counter-flow in a periodic box and the settling of dispersed particles. After the validation, the coagulation process of particles being agitated was simulated with the developed model to investigate the influence of the agitation speed on the coagulation rate.

THEORY

1. Fundamental SPH Theory

1-1. Interpolation

First, we explain the fundamental SPH equations to provide an understanding of the formulation in this work, which is discussed in Section 3. The formulation of an SPH numerical governing equation begins with expressing the function f(**r**) in integral form:

$$f(\mathbf{r}) = \int f(\mathbf{r}')\delta(|\mathbf{r}-\mathbf{r}'|)d\mathbf{r}' \tag{1}$$

where δ is the Dirac delta function and $d\mathbf{r}'$ is a volume element for the space under consideration. Then, f(**r**) can be approximated by replacing δ in Eq. (1) with the kernel function W:

$$f(\mathbf{r}) \cong \langle f(\mathbf{r})\rangle = \int f(\mathbf{r}')W(|\mathbf{r}-\mathbf{r}'|, h)d\mathbf{r}' \tag{2}$$

where h is the smoothing length of W. The smoothing kernel W(r, h) satisfies the following relationships:

$$\int W(|\mathbf{r}|, h)d\mathbf{r} = 1 \tag{3}$$

$$\lim_{h\to 0} W(r, h) = \delta(\mathbf{r}) \tag{4}$$

In SPH, the fluid domain is represented by a set of discretized fluid particles. Each particle carries a small mass, which can be used to approximate Eq. (2) as follows:

$$\langle f(\mathbf{r}_a)\rangle = \sum_b f(\mathbf{r}_b)\frac{m_b}{\rho_b}W(|\mathbf{r}_a-\mathbf{r}_b|, h) \tag{5}$$

where a and b are the particle indices and m and ρ are the mass and density, respectively, of the particle. The summation considers all values of b for which $W(|\mathbf{r}_a-\mathbf{r}_b|, h)$ has a non-zero value. The spatial derivative of f at particle a is also transformed into numerical form by SPH approximation as follows:

$$\left(\frac{\partial f}{\partial \mathbf{r}}\right)_a = \sum_b (f(\mathbf{r}_b)-f(\mathbf{r}_a))\frac{m_b}{\rho_b}\nabla_a W_{ab}(h) \tag{6}$$

where $W_{ab}(h)=W(|\mathbf{r}_a-\mathbf{r}_b|, h)$ and ∇_a denotes the gradient with respect to the coordinates of the particle a. Because W is a known polynomial, $\nabla_a W_{ab}(h)$ can be easily determined; by the approximation of Eq. (6), all of the spatial derivative functions can be transformed into a form that can be solved by computation.

1-2. Equations of Motion: Single-phase Flow

In SPH, the numerical equations of motion are derived by applying Eqs. (5) and (6) to the continuum equations of motion for fluid. The mass conservation equation in partial-differential form is given by

$$\frac{d\rho}{dt} = -\rho\nabla\cdot\mathbf{v} \tag{7}$$

Applying Eq. (6) to $\nabla\cdot\mathbf{v}$ gives

$$\frac{d\rho_a}{dt} = \sum_b m_b\mathbf{v}_{ab}\cdot\nabla_a W_{ab}(\bar{h}_{ab}) \tag{8}$$

where $\bar{h}_{ab}=(h_a+h_b)/2$ and $\mathbf{v}_{ab}=\mathbf{v}_a-\mathbf{v}_b$.

For an inviscid flow without the body force, the conservation of momentum by the pressure term is given by

$$\frac{dv}{dt} = -\frac{\nabla P}{\rho} \tag{9}$$

The right-hand side of Eq. (9) can be expanded by using the following identity:

$$-\frac{1}{\rho}\frac{\partial P}{\partial r} = -\frac{\partial}{\partial r}\left(\frac{P}{\rho}\right) - \frac{P}{\rho^2}\frac{\partial\rho}{\partial r} \tag{10}$$

Approximating the spatial derivative with Eq. (6) and applying it to the right-hand side of Eq. (10) gives

$$-\frac{1}{\rho}\left(\frac{\partial P}{\partial \mathbf{r}}\right)_a = -\sum_b \frac{P_b m_b}{\rho_b \rho_b}\nabla_a W_{ab}(\bar{h}_{ab}) - \frac{P_a}{\rho_b^2}\sum_b \rho_b \frac{m_b}{\rho_b}\nabla_a W_{ab}(\bar{h}_{ab}) \tag{11}$$

Combining Eqs. (9) and (11) gives

$$\left(\frac{d\mathbf{v}}{dt}\right)_a = -\sum_b m_b\left(\frac{P_a}{\rho_a^2}+\frac{P_b}{\rho_b^2}\right)\nabla_a W_{ab}(\bar{h}_{ab}) \tag{12}$$

In weakly compressible SPH, the pressure at the particle a is related to the particle density by the following equation of state:

$$P_a = \frac{c_o\rho_o}{7}\left(\left(\frac{\rho_a}{\rho_o}\right)^7 - 1\right) \tag{13}$$

where c_o is the speed of sound and ρ_o is the reference density of

the fluid. The speed of sound c_o was chosen to be $10\overline{V}_{max}$, where $\overline{V}_{max}$ is the typical speed of the fluid. This means that the relative variation in density is given by $\delta\rho/\rho_o \cong (\overline{V}_{max}/c_o)^2 \cong 0.01$ (e.g., see Monaghan [15] for further details).

In the case of a viscous flow, a viscous force term is added as follows:

$$\left.\frac{d\mathbf{v}_a}{dt}\right|_{visc} = -\sum_b \Pi_{ab} m_b \nabla_a W_{ab} \tag{14}$$

$$\Pi_{ab} = -\frac{\alpha \bar{h}_{ab} c_o}{\bar{\rho}_{ab}} \frac{\mathbf{v}_{ab}\cdot\mathbf{r}_{ab}}{|\mathbf{r}_{ab}|^2} \tag{15}$$

where c is the speed of sound. For the Wendland kernel we used in this work, in the limit that the number of particles becomes infinite, the kinematic viscosity ν is $\alpha c_o h/8$ (see e.g. Monaghan [15] for details).

If the body force that acts on the fluid is included, the final form of the equation for the conservation of momentum is

$$\left(\frac{d\mathbf{v}}{dt}\right)_a = -\sum_b m_b \left(\frac{P_a}{\rho_a^2} + \frac{P_b}{\rho_b^2} + \Pi_{ab}\right) \nabla_a W_{ab}(\bar{h}_{ab}) + \mathbf{g} \tag{16}$$

where $\mathbf{g}$ is the gravitational acceleration. The smoothing length h is related to the particle density by

$$h_a = \sigma \left(\frac{m_a}{\rho_a}\right)^{1/\lambda} \tag{17}$$

where λ is the number of dimensions and σ is a constant that was set to 1.5 in this work. We used a Wendland kernel, which has a support domain of 2h. Thus, the support domain of a particle is three times larger than the initial spacing.

2. DEM Theory

In DEM, predicting the motions of particles begins with Newton's second law:

$$\mathbf{a} = \frac{\mathbf{F}}{m} \tag{18}$$

$$\mathbf{a} = \frac{d\mathbf{v}}{dt} \tag{19}$$

$$\mathbf{v} = \frac{d\mathbf{r}}{dt} \tag{20}$$

Eq. (18) is Newton's second law. Therefore, the force acting on a particle $\mathbf{F}$ should be determined first. For a solid-liquid flow, the contact force, solid-liquid interaction force, and gravitational force are considered:

$$\mathbf{F} = \mathbf{F}^c + \mathbf{F}^l + \mathbf{F}^g \tag{21}$$

Here, $\mathbf{F}^c$ is the contact force, $\mathbf{F}^l$ is the solid-liquid interaction force, and $\mathbf{F}^g$ is the gravitational force.

2-1. Contact Force

Various types of contact relationships can be used to describe the collisions between particles or a particle and wall. The simplest contact model is the linear spring. When contact occurs between two particles or between a particle and wall, the contact force acts on the contact point and affects the motion of the particles. The magnitude of the contact force is calculated with

$$\mathbf{F}^{c(n)} = k_n \Delta\chi_n \hat{\mathbf{n}} + \zeta_n \mathbf{v}_n \tag{22}$$

$$\mathbf{F}^{c(s)} = k_s \Delta\chi_s \hat{\mathbf{s}} + \zeta_s \mathbf{v}_s \tag{23}$$

where n and s are indices for the normal and tangential directions (or components of a vector for those directions), respectively, and $\hat{\mathbf{n}}$ and $\hat{\mathbf{s}}$ are the unit vectors in these directions. k is the contact stiffness, which was assumed to be constant, and ζ is the damping coefficient. $\Delta\chi$ is the overlap, and $\mathbf{v}$ is the relative velocity. To obtain the tangential contact force, a sliding friction term is added to express the incidental friction interactivity. If $|\mathbf{F}^{c(s)}|$ is greater than the maximum friction $\psi|\mathbf{F}^{c(n)}|$, where ψ is Coulomb's coefficient of friction, then sliding occurs. Thus, the resultant tangential force is given by

$$\mathbf{F}^{c(s)} = \min\left(\left|k_s \Delta\chi_s \hat{\mathbf{s}} + \zeta_s \mathbf{v}_s\right|,\ \psi\left|\mathbf{F}^{c(n)}\right|\right)\hat{\mathbf{s}} \tag{24}$$

where k_n, k_s, ζ_n, and ζ_s are material-specific properties. Considering the Hertzian law of contact, the normal stiffness can be related to Young's modulus and Poisson's ratio as follows (e.g., see Misra and Cheung [16] for details):

$$k_n = 0.094 E R \tag{25}$$

$$\frac{1}{E} = \frac{1-\nu_1}{2G_1} + \frac{1-\nu_2}{2G_2} \tag{26}$$

$$\frac{1}{R} = \frac{1}{2R_1} + \frac{1}{2R_2} \tag{27}$$

Here, ν_1 and ν_2 are the Poisson ratios of the two particles, G_1 and G_2 are the Young moduli, and R_1 and R_2 are the radii. The normal and tangential damping coefficients are determined with

$$\zeta_n = -2\ln e \sqrt{\frac{k_n m}{\pi^2 + (\ln e)^2}} \tag{28}$$

$$\zeta_s = -2\ln e \sqrt{\frac{k_s m}{\pi^2 + (\ln e)^2}} \tag{29}$$

$$\frac{1}{m} = \frac{1}{2m_1} + \frac{1}{2m_2} \tag{30}$$

where e is the restitution coefficient and m_1 and m_2 are the masses of the respective particles. In this work, the ratio $k_n : k_s$ was set to 1.5 : 1. In a system dominated by the contact force, the ratio $k_n : k_s$ may influence the simulation result; however, its influence becomes insignificant for a system in which particle inertia is less important, especially for the case of a particles-in-water system.

2-2. Solid-liquid Interaction Force

Solid-liquid interaction occurs as a result of both pressure and drag. The Lagrangian description of the pressure force acting on the solid phase is straightforward:

$$\mathbf{F}_P = -\frac{\nabla P}{\rho_p} \tag{31}$$

where ρ_p is the solid density. Note that $\mathbf{F}_P$ is the force per unit mass. The drag force per unit mass acting on a solid particle is given by

$$\mathbf{F}_D = \frac{K_D}{\rho_p(1-\varepsilon)}(\mathbf{v}_f - \mathbf{v}_p) \tag{32}$$

where ε is the void or volume fraction of the liquid, $\mathbf{v}_p$ is the veloc-

ity of the solid particle, and $\mathbf{v}_f$ is the liquid velocity. K_D is the drag factor and is a function of the liquid density, volume fractions of the solid and liquid, geometry of the solid particle, and relative velocity. In this work, we used Gidaspow's drag model [17], which combines Ergun's equation and Wen and Yu's drag model:

$$K_D=\begin{cases} 150\dfrac{(1-\varepsilon)^2}{\varepsilon}\dfrac{\mu}{d^2}+1.75\dfrac{(1-\varepsilon)\rho_l}{\varepsilon}\dfrac{}{d}|\Delta\mathbf{v}| & (\varepsilon<0.8) \\ \dfrac{3\rho_l\varepsilon(1-\varepsilon)C_D}{4d}|\Delta\mathbf{v}|e^{-2.65} & (\varepsilon\geq 0.8) \end{cases} \tag{33}$$

where $|\Delta\mathbf{v}|=|\mathbf{v}_f-\mathbf{v}_p|$, μ is the dynamic viscosity, d is the diameter of a solid particle, and C_D is the drag coefficient. There are various empirical models for describing C_D. We determined C_D by following Olson's model [18]:

$$C_D=\frac{24}{Re_p}\left(1+\frac{3}{16}Re_p\right)^{1/2} \tag{34}$$

where Re_p is the Reynolds number of the particle:

$$Re_p=\frac{d|\Delta\mathbf{v}|}{\nu} \tag{35}$$

ν is the kinematic viscosity of water and was set to 10^{-6} m^2/s in this work.

FORMULATION OF NUMERICAL GOVERNING EQUATION

In this work, we formulated the SPH governing equation for a two-way coupled solid-liquid flow model. As noted earlier, the most important part of the formulation is an analysis of the interaction between the two phases. The motion of the solid particles on the liquid flow has two effects: (1) the solid particles occupy space, which reduces the flow domain, and (2) the drag and pressure forces act and react according to Newton's third law. Both effects should be considered when developing a two-way coupled solid-liquid flow model.

1. Reduction of Flow Domain by the Solid Particles Occupying Space

The reduction of the flow domain by the solid particles occupying space is represented in the model by revising Eqs. (5) and (6) as follows:

$$\langle f(\mathbf{r}_a)\rangle=\sum_b f(\mathbf{r}_b)\frac{m_b}{\rho_b\varepsilon_b}W(|\mathbf{r}_a-\mathbf{r}_b|, h) \tag{36}$$

$$\left(\frac{\partial f}{\partial \mathbf{r}}\right)_a=\sum_b (f(\mathbf{r}_b)-f(\mathbf{r}_a))\frac{m_b}{\rho_b\varepsilon_b}\nabla_a W_{ab}(\bar{h}_{ab}) \tag{37}$$

The bulk volume of the fluid particle b is replaced by $m_b/\rho_b\varepsilon_b$, which implies that the bulk volume of the equivalent mass of the fluid increases when solid particles are present. This approach enables the summation forms of the equations to satisfy the unity condition in Eq. (3), even when solid particles are present, i.e., $\Sigma_b W_{ab} m_b/\rho_b\varepsilon_b\cong 1$.

As noted, we formulated the SPH model for the solid-liquid flow based on the equations of motion given by Harlow and Amsden [13,14]. The continuum equation for mass conservation is as follows:

$$\frac{d(\rho\varepsilon)}{dt}=-(\rho\varepsilon)\nabla\cdot\mathbf{v} \tag{38}$$

An approximation of Eq. (37) can be applied to the $\nabla\cdot\mathbf{v}$ term on the right-hand side, which transforms Eq. (38) into the following particle-based form:

$$\left(\frac{d(\rho\varepsilon)}{dt}\right)_a=\rho_a\varepsilon_a\sum_b \mathbf{v}_{ab}\cdot\nabla_a W_{ab}(\bar{h}_{ab})\frac{m_b}{\rho_b\varepsilon_b} \tag{39}$$

A similar approach is used to obtain the SPH momentum conservation equation for a solid-liquid flow. The pressure term in the acceleration equation is as follows:

$$\frac{1}{\varepsilon}\frac{dv}{dt}=-\frac{\nabla P}{\rho\varepsilon} \tag{40}$$

The right-hand side of Eq. (40) can be expanded by using the following identity:

$$-\frac{1}{\rho\varepsilon}\frac{\partial P}{\partial \mathbf{r}}=-\frac{\partial}{\partial \mathbf{r}}\left(\frac{P}{\rho\varepsilon}\right)-\frac{P}{\rho^2\varepsilon^2}\frac{\partial(\rho\varepsilon)}{\partial \mathbf{r}} \tag{41}$$

SPH approximation of Eq. (41) gives

$$-\frac{1}{\rho\varepsilon}\left(\frac{\partial P}{\partial \mathbf{r}}\right)_a=-\sum_b\frac{P_b}{\rho_b\varepsilon_b}\frac{m_b}{\rho_b\varepsilon_b}\nabla_a W_{ab}(\bar{h}_{ab}) -\frac{P_a}{\rho_a^2\varepsilon_a^2}\sum_b\rho_b\varepsilon_b\frac{m_b}{\rho_b\varepsilon_b}\nabla_a W_{ab}(\bar{h}_{ab}) \tag{42}$$

Consequently,

$$\left(\frac{d\mathbf{v}}{dt}\right)_a=-\varepsilon_a\sum_b m_a\left(\frac{P_a}{\rho_a^2\varepsilon_a^2}+\frac{P_b}{\rho_b^2\rho_b^2}\right)\nabla_a W_{ab}(\bar{h}_{ab}) \tag{43}$$

2. Determination of Interaction Forces

The pressure and drag terms of interaction force are both determined by SPH interpolation. From Eqs. (31) and (37), the pressure acceleration of a DEM particle i (note that we use the indices i and j for DEM solid particles and a and b for SPH liquid particles hereafter) is interpolated as follows:

$$(\mathbf{F}_P)_i=-\frac{1}{\rho_i}\sum_b\frac{P_b m_b}{\rho_b\varepsilon_b}\nabla_i W_{ib}(h_b) \tag{44}$$

According to Newton's third law, the acceleration of an individual SPH particle a due to its interaction with a solid particle i is as follows:

$$(\mathbf{f}_P)_{ai}=\frac{P_a V_i}{\rho_a\varepsilon_a}\nabla_i W_{ia}(h_a)=-\frac{P_a V_i}{\rho_a\varepsilon_a}\nabla_a W_{ia}(h_a) \tag{45}$$

where V_i is the volume of the solid particle i.

The drag term of the model is formulated by a similar method. To obtain the drag term numerically, we apply the approximation of Eq. (5) to the $K_D(\mathbf{v}_f-\mathbf{v}_p)/(1-\varepsilon)$ term in Eq. (32). The acceleration of the solid particle i by the drag can then be expressed as follows:

$$(\mathbf{F}_D)_i=\frac{1}{\rho_i}\sum_b K_{D(bi)}(\mathbf{v}_b-\mathbf{v}_i)W_{ib}\frac{m_b}{\rho_b\varepsilon_b(1-\varepsilon_b)} \tag{46}$$

From individual fluid particles denoted by a, the solid particle ac-

cumulates the partial drag forces per unit mass as follows:

$$(\mathbf{f}_D)_{ia}=\frac{K_{D(ai)}}{\rho_i}(\mathbf{v}_a-\mathbf{v}_i)W_{ia}\frac{m_a}{\rho_a\varepsilon_a(1-\varepsilon_a)} \tag{47}$$

According to the conservation of momentum, each individual fluid particle a experiences an acceleration of $(\mathbf{f}_D)_{ai}=-(\mathbf{f}_D)_{ia}m_i/m_a$ by interacting with the solid particle i.

3. Determination of Volume Fraction of Fluid ε

It is possible to directly approximate ε for all fluid particles by using Eq. (5). The volume fraction of the fluid at point a is calculated as follows:

$$\varepsilon_a=\sum_q \varepsilon_{0q}W_{aq}\frac{m_q}{\rho_q} \tag{48}$$

$$\varepsilon_{0q}=\begin{cases}1 \text{ if particle q is liquid}\\ 0 \text{ if particle q is solid}\end{cases} \tag{49}$$

The summation subscript q accounts for all of the fluid and solid particles within the support domain; thus, the true volume m_q/ρ_q is applied to the equation instead of the bulk volume $m_q/\rho_q\varepsilon_q$. If no solid particle is within the support domain of the particle a, ε_a is 1. Otherwise, it is less than 1. As described by Eq. (39), we integrate the differential equation for $\rho\varepsilon$ rather than ρ or ε. ρ and ε are therefore calculated by computing Eq. (48) and $\rho=(\rho\varepsilon)/\varepsilon$ in an iterative manner. Numerical tests verified that two iterations give sufficient convergence, which does not affect the overall computational cost.

4. Formulation of Numerical Governing Equation

Finally, the governing SPH equations, which include the full range of interactions between the solid and liquid phases, are obtained as follows:

Mass conservation:

$$\left(\frac{d(\rho\varepsilon)}{dt}\right)_a=\rho_a\varepsilon_a\sum_b \mathbf{v}_{ab}\cdot\nabla_a W_{ab}(\bar{h}_{ab})\frac{m_b}{\rho_b\varepsilon_b} \tag{50}$$

Momentum conservation:

$$\left(\frac{d\mathbf{v}}{dt}\right)_a=-\sum_b m_a\left(\frac{P_a}{\rho_a^2\varepsilon_a}+\frac{\varepsilon_a P_b}{\rho_b^2\varepsilon_b^2}+\Pi_{ab}\right)\nabla_a W_{ab}(\bar{h}_{ab}) +\frac{P_a}{\rho_a\varepsilon_a}\sum_i V_i\nabla_i W_{ib}(h_b)-\frac{1}{\rho_a\varepsilon_a(1-\varepsilon_a)}\sum_j K_{D(aj)}V_j(\mathbf{v}_a-\mathbf{v}_j)W_{aj}+\mathbf{g} \tag{51}$$

For the acceleration of the DEM particles,

$$\left(\frac{d\mathbf{v}}{dt}\right)_i=-\frac{1}{m_i}\sum_j(\mathbf{k}\cdot\Delta\chi_{ij}+\zeta\cdot\mathbf{v}_{ij})-\frac{1}{\rho_i}\sum_b\frac{P_b m_b}{\rho_b\varepsilon_b}\nabla_i W_{ib}(h_b) -\frac{1}{\rho_i}\sum_b K_{D(bi)}(\mathbf{v}_b-\mathbf{v}_i)\frac{m_b}{\rho_b\varepsilon_b(1-\varepsilon_b)}W_{ib}+\mathbf{g} \tag{52}$$

In Eqs. (51) and (52), all terms other than the external self-gravity **g** conserve momentum exactly.

5. Time Stepping

Eqs. (50)-(52) are solved numerically by using a mid-point integrator. Note that the acceleration equation only is integrated for DEM particles, whereas both the acceleration and continuity equations are solved for SPH particles. At the beginning of each time step, the predicted values of **v** and $\rho\varepsilon$, which are denoted by the superscript *, are calculated to determine the derivatives as follows:

$$\mathbf{v}^{*\xi}=\mathbf{v}^{\xi-1/2}+\frac{\Delta t}{2}\left(\frac{d\mathbf{v}}{dt}\right)^{\xi-1}$$
$$(\rho\varepsilon)^{*\xi}=(\rho\varepsilon)^{\xi-1/2}+\frac{\Delta t}{2}\left(\frac{d(\rho\varepsilon)}{dt}\right)^{\xi-1} \tag{53}$$

where ξ is the time step index. The rates of change can now be calculated because they depend on known quantities. After $\rho^{*\xi}$ and $\varepsilon^{*\xi}$ are determined as described in section 3.3, the time derivatives of $\rho\varepsilon$ and **v** are determined as follows:

$$\left(\frac{d(\rho\varepsilon)}{dt}\right)^{\xi}=\frac{d(\rho\varepsilon)}{dt}(\mathbf{r}^{\xi},\mathbf{v}^{*\xi},h^{*\xi},(\rho\varepsilon)^{*\xi})$$
$$\left(\frac{d\mathbf{v}}{dt}\right)^{\xi}=\frac{d\mathbf{v}}{dt}(\mathbf{r}^{\xi},\mathbf{v}^{*\xi},\ldots) \tag{54}$$

The quantities $\rho\varepsilon$ and **v** at the end of the step are then given by

$$\mathbf{v}^{\xi+1/2}=\mathbf{v}^{\xi-1/2}+\Delta t\left(\frac{d\mathbf{v}}{dt}\right)^{\xi}$$
$$\rho\varepsilon^{\xi+1/2}=\rho\varepsilon^{\xi-1/2}+\Delta t\left(\frac{d(\rho\varepsilon)}{dt}\right)^{\xi} \tag{55}$$

The particle position is finally updated.

$$\mathbf{r}^{\xi+1}=\mathbf{r}^{\xi}+\Delta t\left(\frac{d\mathbf{v}}{dt}\right)^{\xi+1/2} \tag{56}$$

TEST AND VALIDATION

The developed model was implemented into a computer code. Tests were done in a two-dimensional xz domain, where the coordinates were set so that gravity acted in the $-\hat{z}$ direction.

1. Liquid-solid Drag in Periodic Box

The liquid-solid interaction is affected by both pressure and drag. Before the combined effect of the two factors was investigated, the formulated drag term was independently tested by simulating the liquid and solid flows in opposite directions in a periodic box. The test case involved DEM solid particles and SPH liquid particles moving along the x axis with initial velocities of −5 and 1 m/s, respectively. Fig. 1 shows a schematic of the problem setup. The DEM solid particles and SPH liquid particles were uniformly set up in a 1 m×1 m periodic domain. Forty thousand SPH parti-

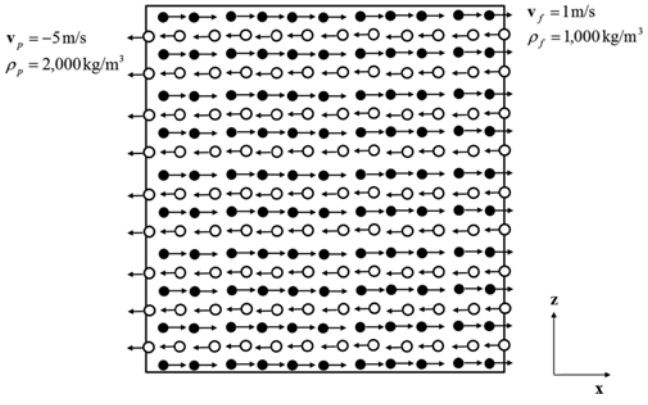

Fig. 1. Schematic of test case: liquid-solid drag in a 2D periodic box. The black dots are DEM solid particles, and the white dots are SPH liquid particles.

cles were used for the simulation. The diameter of the DEM particles was set to 0.005 m, and the solid density was set to 2,000 kg/m^3. The number of DEM particles varied between 1024 and 8464, which corresponds to a ratio of initial momentums for the solid and liquid of ~0.2-2. Because the system was assumed to be homogeneous, there was no pressure or velocity gradient, and only the drag term was considered.

The acceleration equation with only the drag term is as follows:

$$\frac{d\mathbf{v}_f}{dt} = -\frac{K_D(\mathbf{v}_f - \mathbf{v}_p)}{\rho_f \varepsilon} \tag{57}$$

$$\frac{d\mathbf{v}_p}{dt} = -\frac{K_D(\mathbf{v}_f - \mathbf{v}_p)}{\rho_s (1-\varepsilon)} \tag{58}$$

For comparison with the SPH simulation result, Eqs. (57) and (58) were solved numerically with a mid-point integrator. Eq. (33) was also solved during the computation because K_D is dependent on $\mathbf{v}_f$ and $\mathbf{v}_p$ and therefore varies with time.

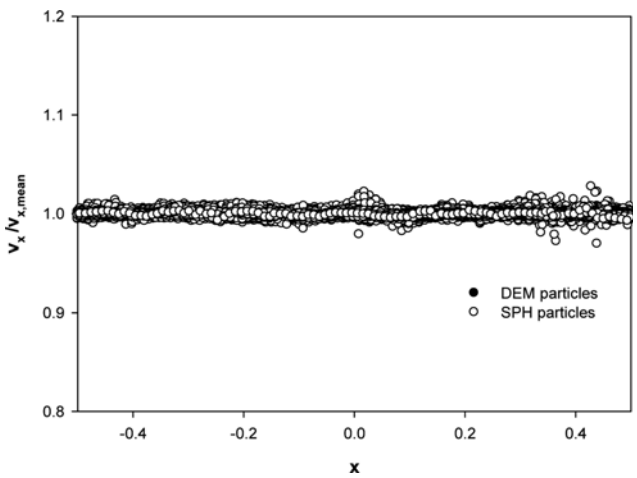

Fig. 2. Velocity profile of particles at t=3 s: $(M_p/M_f)_{(t=0)}$=0.5. Velocities of individual particles v_x are scaled through division by the mean value $v_{x,mean}$.

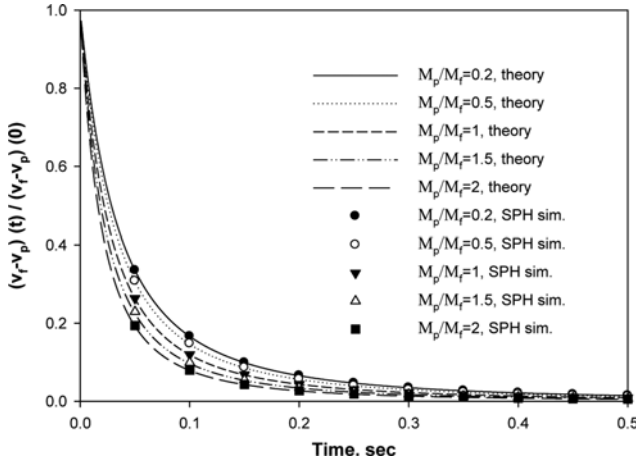

Fig. 3. Velocity as a function of time. The scattered points correspond to simulations, and the lines indicate solutions with Eqs. (57) and (58).

Fig. 2 shows the resultant velocities for all individual SPH and DEM particles at t=3 s when $(M_p/M_f)_{(t=0)}$=0.5. The homogeneity of the system was well represented in the simulation, and the velocity deviation was less than 3%.

Fig. 3 shows the time-dependent velocity difference between particles and fluid according to the simulation and theory. Velocities were calculated by averaging all particles. The numerical simulation results showed strong agreement with the theory. Under all conditions, the time-dependent velocity in the simulation agreed very well with the theory.

2. Settling of Numerous Solid Particles in Infinite Liquid

The settling of solid particles in an infinite water body was simulated to validate the model. Increasing the solid volume fraction is known to decrease the terminal settling velocity of particles owing to the interaction between the two phases. The derivation of the equations for this system was described by Monaghan [19]. When a solid particle settles at the terminal velocity, the momentum equations of the liquid and solid are as follows:

$$-\frac{1}{\rho_f}\frac{\partial P}{\partial z} + g + \frac{K_D(v_p - v_f)}{\rho_f \varepsilon} = 0 \tag{59}$$

$$-\frac{1}{\rho_p}\frac{\partial P}{\partial z} + g - \frac{K_D(v_p - v_f)}{\rho_p (1-\varepsilon)} = 0 \tag{60}$$

Eliminating $\partial P/\partial z$ from the two above equations produces a linear equation with the two variables v_f and v_p. If the flow is incompressible, i.e., $(1-\varepsilon)v_p + \varepsilon v_f = 0$, the algebraic calculation of the equation consequently gives the terminal velocity of the solid particles and the counter-flow velocity of the liquid.

$$v_f = \frac{g\varepsilon(1-\varepsilon)^2(\rho_p - \rho_f)}{K_D} \tag{61}$$

$$v_p = -\frac{g\varepsilon^2(1-\varepsilon)(\rho_p - \rho_f)}{K_D} \tag{62}$$

Given that K_D is also a function of v_f and v_p, the analytic terminal settling velocity of particles and the counter-flow velocity are determined by computing Eqs. (33), (61), and (62) iteratively.

For the test, a 3D domain with the dimensions of 0.5 m×0.5 m×1 m (−0.25 m<x, y<0.25 m, −0.5 m<z<0.5 m) initially filled with a homogeneous particle-water mixture was set up. Two million SPH liquid particles were used for the simulation. The diameter of the DEM solid particles was set to 0.005 m, and the number of particles was varied between 8192 and 390,224. A periodic boundary along the x and y axes, solid boundary for the bottom, and free upper surface boundary were applied. For the DEM particles, the bottom solid boundary wall exerted a repulsive contact force that prevented the particles from penetrating the wall. For SPH particles, the boundary consisted of three layers of boundary particles. These boundary particles were regarded to be the same as real liquid particles with regard to material properties such as the density and pressure, but they were fixed on space. ρ_s and ρ_l were set to 1,100 and 1,000 kg/m^3, respectively.

Fig. 4 shows snapshots of the particle settling and the distributions of the resultant solid fractions under the condition $1-\varepsilon_o \cong 0.02$ (corresponding to the 78,608 DEM particles), where $1-\varepsilon_o$ is the initial volume fraction of solid. Three regimes formed due to

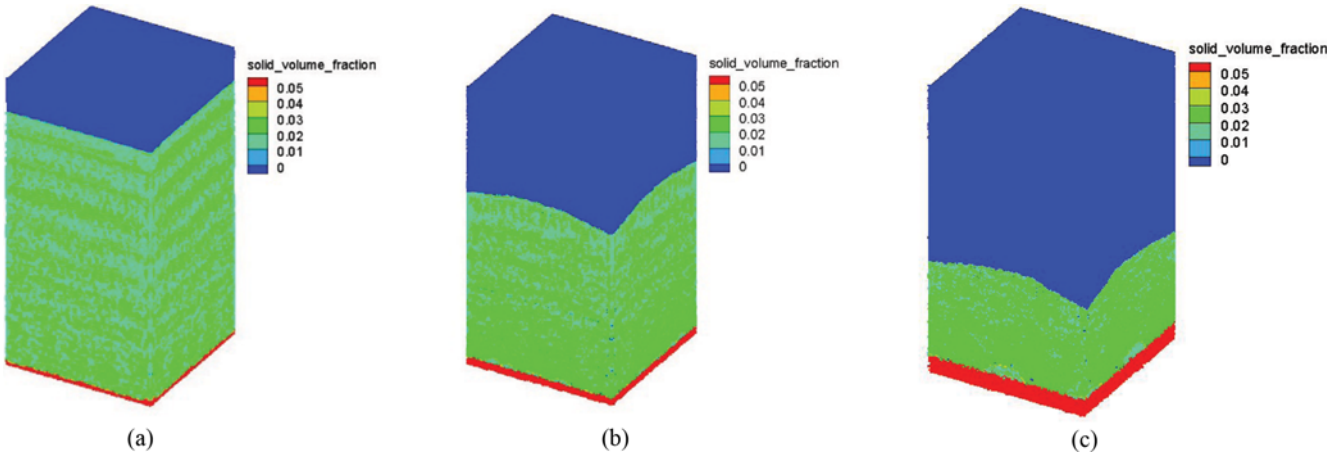

Fig. 4. Sedimentation and resultant change in the distribution of the solid volume fraction (on SPH particles): 1-ε_o=0.02 at (a) t=1 s, (b) t=3 s, and (c) t=5 s.

sedimentation. The top regime was free of the solid fraction (i.e., supernatant); the solid particles settled on the bottom to form a close packing bed (i.e., packed-bed regime). In between was another regime in which the local volume fraction of solid was equivalent to the initial value and particles in the regime settled to form a plug flow (i.e., intermediate regime).

Under the conditions employed in this test, the settling velocity of particles converged sufficiently close to the terminal velocity in less than 0.4 s. Therefore, we measured the velocities of the SPH and DEM particles after 2 s under the assumption that the sedimentation velocity in the intermediate regime reached the terminal velocity and compared them to v_p and v_f obtained analytically with Eqs. (61) and (62). After 2 s of simulation, we obtained $\bar{z}$, which is the average of the z coordinates of DEM particles. Assuming that $\bar{z}$ was close enough to the *z*-directional center of the intermediate regime (or far enough from the floor and upper boundary of the regime), we chose particles that were located at $|z-\bar{z}|\leq 2h$, and the average velocities of the SPH and DEM particles were regarded as the terminal settling velocity and counter-flow velocity, respectively. The velocities were than compared to the values of v_p and v_f that were obtained analytically.

Fig. 5 shows the terminal settling velocities of the DEM particles and the corresponding counter-flow velocities of the SPH particles with various initial volume fractions. For all of the volume fraction conditions considered in this work, the terminal settling velocity of solid particles and counter-flow velocity of the liquid from the simulation agreed well with those obtained by Eqs. (61) and (62). The results showed that the SPH-DEM model computed the interaction between the two phases well.

3. Settling of Numerous Solid Particles in the Infinite Liquid

In the SPH algorithm, a value at a certain point is interpolated from the values at neighboring points. Thus, for a mesoscale coupling of SPH with DEM, the relationship between the ranges of an appropriate SPH particle resolution with the diameter of DEM particles needs to be verified. We conducted a test similar to that described in section 4.2 with various SPH particle resolutions. The initial spacing of the SPH fluid particles dp_{sph} was varied between one-third and three times the DEM particle diameter d_{dem}, which

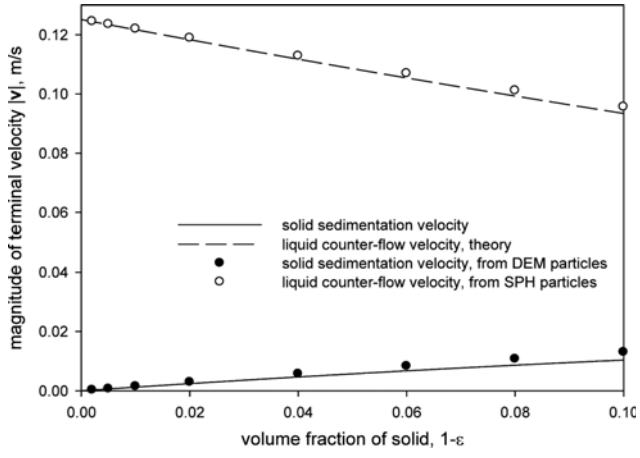

Fig. 5. Settling velocity (solid) and counter-flow velocity (liquid) as a function of time. Scattered points correspond to simulations, and lines indicate analytical solutions.

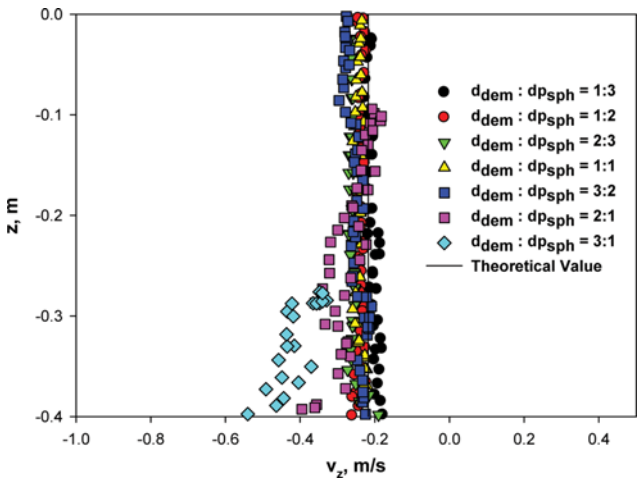

Fig. 6. Settling velocity profile of the DEM particles in the dispersed (intermediate) regime.

was set to 0.01 in this test. All of the tests were carried out by using an initial liquid volume fraction of ~0.95. We analyzed the results by investigating the vertical (*z*-axial) profiles of the velocity and volume fraction. The particles located at $\sqrt{|x|^2+|y|^2}<h$ were used as monitoring particles.

Fig. 6 shows the velocity profile of DEM particles in the dispersed regime at t=2 s with various particle resolutions. When $dp_{sph} \leq 1/2d_{dem}$, the sedimentation velocity became very noisy and faster than the expected value by theory. We assumed that the main cause was that the approximation in Eq. (48) was no longer valid under the condition of an overly fine SPH resolution ($dp_{sph}=1/3d_{dem}$ and $dp_{sph}=1/2d_{dem}$), and the interpolation in Eq. (44) did not satisfy the unity condition of the SPH summation. We used $3dp_{sph}$ as the support domain of an SPH particle, which is still larger than the radius of a DEM particle for those cases. However, the numerical error in Eq. (48) can increase with d_{dem}/dp_{sph}. Based on the numerical test results, we concluded that the initial SPH particle spacing should be greater than $0.5d_{dem}$. When $dp_{sph}>0.5d_{dem}$, the settling velocity of the solid particles agreed reasonably well with those obtained by using Eq. (41).

The liquid volume fraction ε was interpolated by using the pairs between SPH and DEM particles. Therefore, the resolution ratio of SPH to DEM may play a significant role in calculating ε. Fig. 7 shows the resultant vertical void fraction profile from SPH particles within the range of $\sqrt{|x|^2+|y|^2}<h$. The test results showed that the interpolation of ε in the packed-bed regime when $dp_{sph} \geq 2d_{dem}$ caused a significant error, although the interpolation in the intermediate regime gave a reasonable result. In the packed-bed regime, the simulation results when $dp_{sph} \geq 2d_{dem}$ produced the incorrect volume fraction profile given that the upper limit of the solid volume fraction of the packed bed consisting of monosized particles was ~0.6.

As discussed above, the test results showed that the sedimentation velocity in the dispersed regime was ill-calculated at an overly fine SPH resolution ($dp_{sph} \leq 1/2d_{dem}$), whereas the volume fraction in the packed regime was ill-calculated under the opposite condition of the coarse resolution of SPH particles ($dp_{sph} \geq 2d_{dem}$). Thus, we concluded that the appropriate range of the ratio of the SPH particle resolution to the particle initial spacing is approximately $2/3 \leq dp_{sph}/d_{dem} \leq 3/2$. Note that this range is limited to the case of using a Wendland kernel with the support domain of $|r|<2h$.

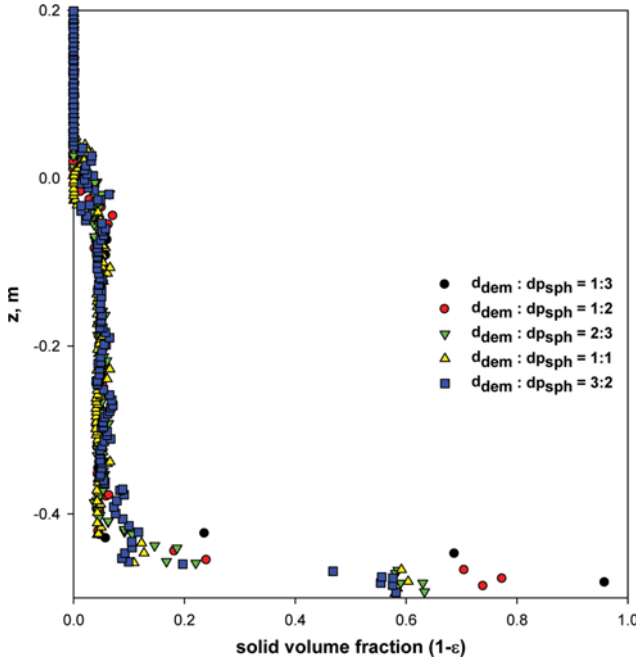

Fig. 7. Solid volume fraction profile from SPH particles. In the packed regime, the solid volume fraction profiles calculated from d_{dem} : dp_{sph}=1 : 3 and d_{dem} : dp_{sph}=1 : 2 was overestimated.

APPLICATION OF THE MODEL SIMULATING THE AGITATION-COAGULATION PROCESS

1. Simulation Methods

The developed two-way coupled SPH-DEM model was used to simulate the coagulation process in a propeller-type agitator. Coagulation refers to the formation of larger particles by the aggregation of primary fine particles through contact. In water treatment processes, coagulation is used to effectively remove dispersed fine particles. A slurry has a large number of particles dispersed within the liquid. Agitation enhances the contact between these particles, which causes them to grow into larger particles and makes it eas-

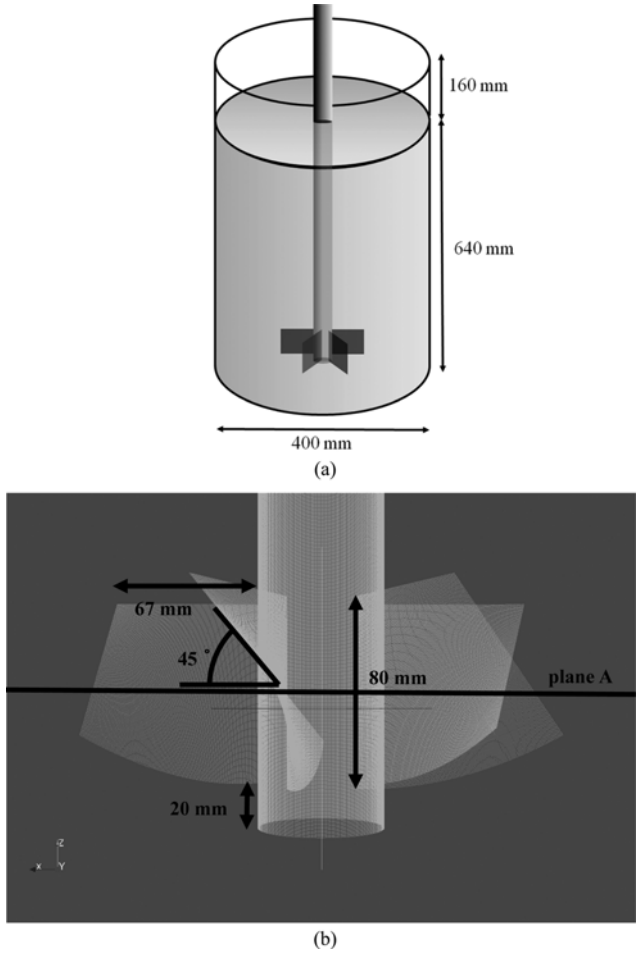

Fig. 8. Geometry of (a) the entire agitator and (b) propeller.

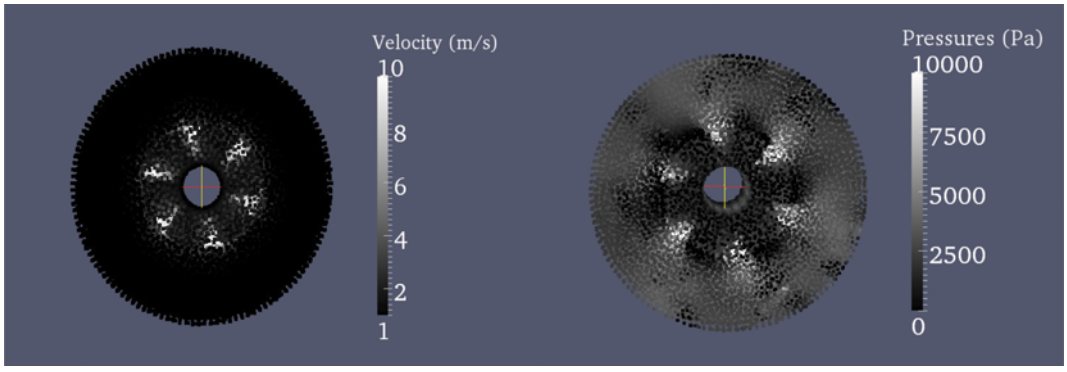

Fig. 9. Simulation result: (a) velocity and (b) pressure distribution of the water at z=60 mm (t=1 s, ω_o=116.7 rad/s).

ier to separate them from the liquid or to recover them.

Fig. 7 shows the geometric conditions applied in this work. A cylinder with a diameter of 400 mm and height of 800 mm was 80% filled with water (Fig. 8(a)). In the agitating unit, six propellers were attached to a rod with a diameter of 60 mm. For each propeller, the width and height were set to 67 and 80 mm, respectively. Generally, a propeller in an agitator is designed to have a distortion angle rather than remain flat in order to induce a turbulent flow and increase the coagulation efficiency by introducing a z-directional component of the flow. In this work, virtual particles were arranged to set the distorted angle of each propeller to 45° (Fig. 8(b)). The thickness of the propeller was not considered; thus, it was possible to satisfy the no-slip condition along the propeller simply by setting the velocities of the virtual particles on the propeller to the rotational velocities at each point.

Two thousand DEM solid particles were set in the water phase, which was represented by 76,000 SPH particles. To investigate the influence of the rotational speed on the coagulation efficiency, the rotational speed was varied within the range of 50-116.7 rad/s. The particle sizes and densities were randomly distributed within a range of 300-10,000 μm and 995-1,005 kg/m^3, respectively. The initial positions of the particles were also randomly distributed within the liquid. To determine the DEM contact force, Young's modulus and Poisson ratio were set to 200 GPa and 0.3, respectively. In all cases, the simulation was conducted for 5 s. For simplicity, the material properties were equally applied to the walls and particles.

There are two fundamental models to describe the coagulation process: the rapid coagulation model by Smoluchowski [20], and the slow coagulation model by Fuchs [21]. The energy barrier introduced through the net inter-particle repulsive force is considered in the slow coagulation model, while it is neglected in the rapid coagulation model. Via the energy barriers, colloidal particles in a liquid are dispersed, and the energy barrier increases with the surface potential. Generally, the surface potential can be neutralized by adding a specific electrolyte or controlling the pH. In this work, for simplicity, we assumed the absence of repulsive force with a fully neutralized surface potential. Thus, the rapid coagulation model was applied.

In the absence of a repulsive energy barrier, two particles coming into contact results in coagulation. When primary particles i and j coagulate, the properties of the resultant particle τ are determined as follows:

$$m_\tau = m_i + m_j \tag{63}$$

$$r_\tau = (r_i^3 + r_j^3)^{1/3} \tag{64}$$

$$\rho_\tau = \frac{r_i^3\rho_i + r_j^3\rho_j}{r_i^3 + r_j^3} \tag{65}$$

$$\mathbf{v}_\tau = \frac{m_i\mathbf{v}_i + m_j\mathbf{v}_j}{m_i + m_j} \tag{66}$$

where m is the mass, r is the radius, ρ is the density, and **v** is the velocity. Eqs. (63)-(65) come from the conservation of mass, and Eq. (66) comes from the conservation of momentum.

2. Simulation Results

2-1. Flow Analysis

In the simulation results, the development of the fluid velocity and pressure distribution occurred at a fast rate, and the flow reached a steady state within 1 s. Fig. 9 shows the velocity and pressure distribution along the plane across the center of the propeller (plane A in Fig. 8(b)). High pressure was observed along the boundary of the propellers due to the resistance of the fluid to the surface of the propellers. Outside the boundary of the propeller blades, a lower hydrostatic pressure was observed in a higher-speed region, which corresponds well to Bernoulli's theorem.

Fig. 10 shows the velocity distributions with respect to the distance from the rotational axis. Under three different rotational

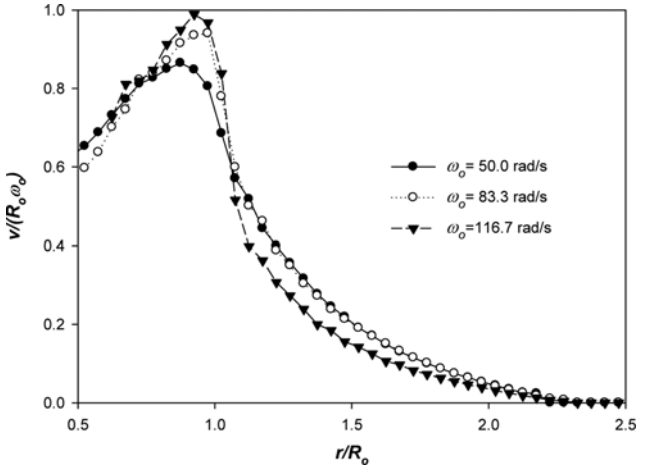

Fig. 10. Simulation result: Water velocity as a function of r. Values are averaged.

speed conditions, the dimensionless velocity $|\mathbf{v}|/R_o\omega_o$ showed similar distributions as a function of r. Under a high rate of revolution (e.g., ω_o=116.7 rad/s), the velocity decreases slightly more drastically with increasing distance from the center. At ω_o=116.7 rad/s, the deviation in the velocity increased, which corresponds well to the current understanding that flow irregularity increases with an inertia-dominant flow.

2-2. Coagulation Analysis

During agitation, solid particles are dragged by the fluid flow. A velocity difference is then introduced to the motion of particles according to their size. This enhances the contact between the particles, the coagulation of the particles, and the resultant growth into larger particles. The agitation speed may play an important role in the coagulation kinetics. In this work, an SPH-DEM simulation was performed to investigate the influence of the agitation speed on the coagulation efficiency.

In the rapid coagulation model, if the probability distribution of the particle displacement is uniform, there is a second-order kinetic relationship between the particle number and coagulation rate:

$$\frac{dN}{dt} = -k_r N^2 \tag{67}$$

Here, N is the total number of solid particles, and k_r is the coagulation rate constant. Eq. (67) can be easily solved to obtain N as a function of time:

$$\frac{1}{N(t)} - \frac{1}{N_o} = k_r t \tag{68}$$

If the motion of a particle is dominated by Brownian motion (e.g., coagulation of a colloidal particle with no advective flow), a uniform probability distribution of the particle location along the radial direction is a reasonable assumption. For a mildly convecting flow, the probability is nearly uniform at the early stage of the convection but gradually becomes non-uniform with time. If particles range in size from several hundreds of micrometers to several millimeters in a strongly advective flow, the probability distribution of the particle's location will become non-uniform in a relatively short amount of time, and the number of particles as a function of time may not follow Eq. (68).

Fig. 11 shows the change in the number of particles with time. At a relatively low revolution speed, the linear regression between t and $1/N(t)-1/N_o$ produced a high degree of correlation (R^2=0.9986 at ω_o=50 rad/s and R^2=0.9944 at ω_o=83.3 rad/s). However, when ω_o=116.7 rad/s, the coagulation kinetics did not follow Eq. (68) well. Under this condition, the coagulation rate decreased with time, even when it was high during the early stages.

To investigate the main cause of this result, the particle distribution of the location with time was observed. We divided the region into two parts with equivalent volumes: the inner half and outer half. Provided that the probability distribution of the particle location was uniform everywhere, the particle location probabilities in the inner and outer halves were 50% in each case. Fig. 12 shows the fraction of particles reported in the outer half at t=3 s. Because of the centrifugal effect, the fraction of particles in the outer half slightly exceeded 50% at all size intervals. When ω_o=50 rad/s and ω_o=83.3 rad/s, the fraction in the outer half varied within the range of 55%-70% and did not vary significantly according to the size

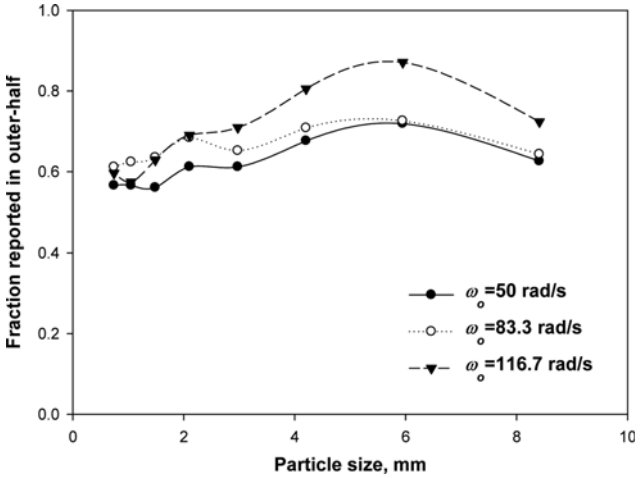

Fig. 12. Coagulation result: Fraction of particles reported in the outer half at t=3 s.

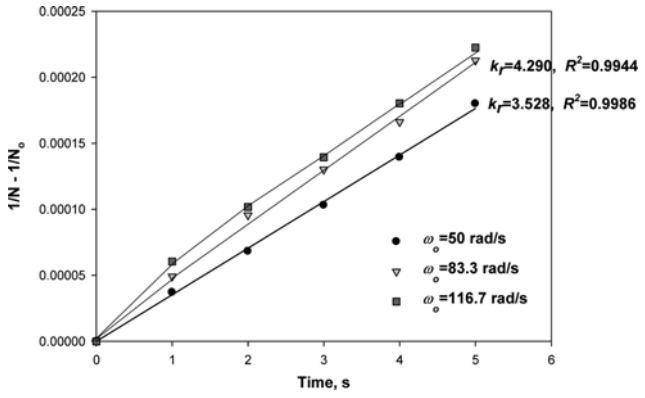

Fig. 11. Coagulation result: change in the number of particles. When ω_o=116.7 rad/s, the kinetics does not follow the second-order kinetic relationship well, and the coagulation rate decreases over time.

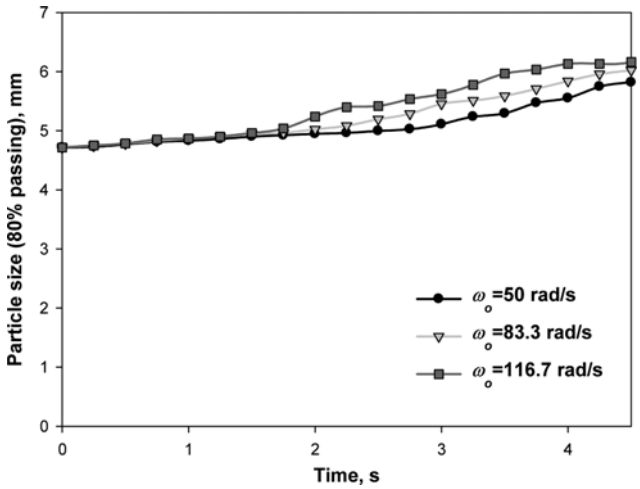

Fig. 13. Coagulation result: change in ν with time.

interval. However, when ω_o=116.7 rad/s, the fraction increased significantly in the coarse particle range, which was obviously a result from the size separation effect of centrifugation. The main purpose of agitation in a coagulation process is to enhance the contact between particles by using the velocity difference of the particle motions in the fluid. At high-speed revolution, the difference in particle motions is enhanced. However, the simulation results showed that, if the revolution speed exceeds a certain range, a size separation effect arises that interferes with the contact between the particles. An analysis of the 80% passing size with time showed a similar tendency (Fig. 13). When ω_o=116.7 rad/s, the growth of the particles slowed with time, although it was relatively rapid during the early stages.

CONCLUSION

We developed a new two-way coupled SPH-DEM model by using multiphase flow dynamics. The model considers (1) the reduction of the flow domain due to the space occupied by the solid particles, and (2) the action/reaction of the drag and pressure forces. Therefore, it can be used to represent the interactions between the solid and liquid phases in both cases. To validate the model, a solid-liquid counter-flow in a periodic box and the settling of dispersed particles were simulated by using various volume fractions. The results of both simulations were in very good agreement with the analytical results. We considered the resolution and verified that the initial SPH particle spacing should be between 0.5 and 1.5 times of the DEM particle diameter.

The developed model was applied to simulating the coagulation process by agitation. The results showed that, at a high revolution speed, the coagulation rate decreases with time, and overly fast agitation can have an adverse effect on the coagulation efficiency. The developed model is considered to be applicable to the design of various types of solid-liquid two-phase flows.

In the model, the two phases interact with each other in terms of both the drag and pressure; however, some inertia-related forces such as shear lift have different origins and have not been incorporated in the model. These forces sometimes play a significant role in the dynamics and need to be incorporated for a complete description of the solid-liquid interaction. We intend to consider this aspect in future work.

ACKNOWLEDGEMENTS

This research was supported by the Basic Science Research Program through the National Research Foundation of Korea (NRF) funded by the Ministry of Science, ICT & Future Planning (2015R1A2A1A15056229) and by the Nuclear Safety Research Program through the Korea Radiation Safety Foundation (KORSAFe) and Nuclear Safety and Security Commission (NSSC), Republic of Korea (Grant No. 1403005).

SUPPORTING INFORMATION

Additional information as noted in the text. This information is available via the Internet at http://www.springer.com/chemistry/journal/11814.

NOMENCLATURE

C_D : drag coefficient
c_o : speed of sound
dp_{sph} : initial spacing of the SPH particles
d_{dem} : diameter of the DEM particles
e : restitution coefficient
$\mathbf{F}$: force acting on a particle
$\mathbf{F}^c$: contact force
$\mathbf{F}^{c(n)}$: normal contact force
$\mathbf{F}^{c(s)}$: tangential contact force
$\mathbf{F}_P$: pressure force per unit mass
$\mathbf{F}_D$: drag force per unit mass
$\mathbf{F}^l$: solid-liquid interaction force
$\mathbf{F}^g$: gravitational force
$(\mathbf{f}_P)_{ai}$: acceleration of an individual SPH particle a due to its interaction with a solid particle i
G_1, G_2 : Young's modulus
$f(\mathbf{r})$: function defined at $\mathbf{r}$
$\mathbf{g}$: gravitational acceleration
h : smoothing length
K_D : drag factor
k : contact stiffness
k_n : normal spring stiffness
k_r : coagulation rate constant
k_s : tangential spring stiffness
M_p/M_f : ratio of the initial momentum of solid and liquid
m : particle mass
N(t) : total number of solid particles
N_o : initial number of solid particles
n : index indicating the normal direction
$\hat{\mathbf{n}}$: unit normal vector
s : index indicating the tangential direction
P : liquid pressure
P_a : pressure at particle a
R : radius of DEM particle
R^2 : coefficient of determination
R_o : radial distance from the center to the tip of the propeller
Re_p : reynolds number of the particle
r : radius of the DEM particle a
$\hat{\mathbf{s}}$: unit tangential vector
V_i : volume of the solid particle i
$\overline{V}_{max}$: typical speed of the liquid
$\mathbf{v}$: velocity
$\mathbf{v}_a$: velocity at particle a
$\mathbf{v}_{ab}$: $\mathbf{v}_a - \mathbf{v}_b$
$\mathbf{v}_f$: liquid velocity
$\mathbf{v}_p$: velocity of the solid particle
v_f : speed of liquid
v_p : speed of solid
$(|\mathbf{r}-\mathbf{r}'|, h)$: smoothing kernel function
$\mathbf{r}$: position vector
$\mathbf{r}'$: position vector in integral; see Eq. (1)
α : coefficient for the artificial viscosity

δ : dirac delta function
ε : void fraction
∇_a : gradient with respect to the coordinates of particle a
ρ_a : density at particle a
ρ : liquid density
Π_{ab} : artificial viscosity
λ : number of dimensions
ζ : damping coefficient
$\Delta\chi$: overlap
ψ : Coulomb's coefficient of friction
$\Delta\chi_n$: normal displacement of the overlap
$\Delta\chi_s$: tangential displacement of the overlap
ρ_p : solid density
ρ_l : liquid density
μ : dynamic viscosity
ν : kinematic viscosity
ε_a : void fraction at particle a
V_i : volume of the solid particle i
ξ : time step index
ρ^* : temporary density used at a time step
ε^* : temporary void fraction used at a time step
ω_o : rotational speed of the propeller

REFERENCES

1. Y. Tsuji, T. Tanaka and T. Ishida, *Powder Technol.*, **71**, 239 (1992).
2. T. Kawaguchi, T. Tanaka and Y. Tsuji, *Powder Technol.*, **96**, 129 (1998).
3. B. Hoomans, *Chem. Eng. Sci.*, **51**, 99 (1996).
4. B. Hoomans, J. A. M. Kuipers and W. P. M. van Swaaij, *Powder Technol.*, **109**, 41 (2000).
5. B. Wang, D. L. Xu, K. W. Chu and A. B. Yu, *Appl. Math. Model.*, **30**, 1326 (2006).
6. M. Lungu, J. Sun, J. Wang, Z. Zhu and Y. Yang, *Korean J. Chem. Eng.*, **31**, 1148 (2014).
7. L. B. Lucy, *The Astronomical J.*, **82**, 1013 (1977).
8. R. A. Gingold and J. J. Monaghan, *Mon. Not. R. Astron. Soc.*, **181**, 375 (1977).
9. A. V. Potapov, M. L. Hunt and C. S. Campbell, *Powder Technol.*, **116**, 204 (2001).
10. P. W. Cleary, M. Sinnot and R. Morrison, *Miner. Eng.*, **19**, 1517 (2006).
11. M. Robinson, S. Luding and M. Ramaioli, *Int. J. Multiph. Flow*, **59**, 121 (2013).
12. T. B. Anderson and R. Jackson, *Ind. Eng. Chem. Fundam.*, **6**, 527 (1967).
13. F. H. Harlow and A. A. Amsden, *J. Comput. Phys.*, **17**, 19 (1975).
14. F. H. Harlow and A. A. Amsden, *J. Comput. Phys.*, **18**, 440 (1975).
15. J. J. Monaghan, *Report on Progress in Physics*, **6**, 1703 (2005).
16. A. Misra and J. Cheung, *Powder Technol.*, **105**, 222 (1999).
17. D. Gidaspow, *Multiphase flow and fluidization: Continuum and Kinetic Theory Description*, Academic Press, San Diego (1994).
18. R. M. Olson, *Essentials of Engineering Fluid Mechanics, International Textbook Company*, Scranton, Pennsylvania (1960).
19. J. J. Monaghan, *J. Comput. Phys.*, **138**, 801 (1997).
20. M. V. Smoluchowski, *Zeitschrift für Physikalische Chemie*, **92**, 129 (1917).
21. N. Fuchs, *Z. Phys. Chem.*, **89**, 736 (1934).